



Evaluation of the role of hatch-spacing variation in a lack-of-fusion defect prediction criterion for laser-based powder bed fusion processes

Ryan Harkin¹ · Hao Wu^{1,2} · Sagar Nikam¹ · Shuo Yin³ · Rocco Lupoi³ · Patrick Walls⁴ · Wilson McKay⁴ · Shaun McFadden¹

Received: 3 November 2022 / Accepted: 23 February 2023 / Published online: 3 March 2023
© The Author(s) 2023

Abstract

Lack of fusion (LOF) defects impact adversely on the mechanical properties of additively manufactured components produced via laser-based powder bed fusion. Following a stress-relieving heat treatment, the tensile properties and hardness of Ti6Al4V components were found to be negatively impacted by the presence of LOF defects. This work considers a geometrical-based inequality for the prediction of LOF defects. We critically evaluate an LOF criterion using both the experimentally and analytically obtained melt pool geometries. Experimentally, we determined melt pool dimensions by analysing a single-layer, multi-track deposition with oversized hatch spacing in order to establish depth and width from non-overlapping melt pools. Analytically, Rosenthal-based predictions of melt pool size (width and depth) are applied. To investigate LOF defects, we used hatch spacing as the main parameter variation to investigate defects while keeping all other controllable parameters unchanged. An original LOF criterion from the literature was found to be an adequate predictor of LOF defects when experimentally obtained melt pool geometry was used. Critically, however, the analytical expressions for melt pool geometry were found to be in error and this caused the LOF criterion to fail in predicting LOF defects in all cases where defects were observed experimentally. However, an adaptation to the LOF prediction criterion is proposed whereby it is recommended that a correction factor $R_c^2 = 0.7$ (or $R_c = 0.83$) is used with the analytically derived melt pool geometry. Furthermore, this correction is extended into the laser power versus scanning speed operating space to give minimum (corrected) line energy for LOF avoidance in Ti6Al4V components.

Keywords Defects · Titanium alloy · Additive manufacturing · Powder bed fusion

1 Introduction

Parameter selection in laser-based powder bed fusion (L-PBF) influences the quality of as-built parts. High-density, low-defect components are desirable because they reduce

the requirements for post-processing such as hot isostatic pressing (HIP) [1][1]. Suboptimal processing in L-PBF leads to the systematic generation of internal defects. Systematic defects include lack of fusion (LOF) flaws, when line energy is too low, and keyhole porosity, when line energy is too high [3]. To avoid systematic defects, laser power, P , and scan speed, V , should be selected to give a stable melt pool controlled by heat conduction (known as a conduction-mode operation). Hence, optimal process parameters are defined within an operating window on a P – V plot [4]. However, stochastic (or random) defects are sometimes present. Stochastic defects have been attributed to residual gas porosity, that is, gas pores originally present in the feedstock powder that survive the L-PBF process. It has been estimated that approximately 10% of the initial porosity defects in powder survive as porosity in the as-built component [4].

✉ Shaun McFadden
s.mcfadden2@ulster.ac.uk

¹ School of Computing, Engineering, and Intelligent Systems, Ulster University, Derry, UK

² Present Address: School of Metallurgy and Materials, University of Birmingham, Birmingham, UK

³ Department of Mechanical, Manufacturing and Biomedical Engineering, Trinity College Dublin, Dublin, Ireland

⁴ Laser Prototypes Europe Ltd, Prince Regent Rd, Belfast, UK

Most commercial machines have pre-defined proprietary databases of parameters with the intention of maximising the quality of the as-built product. However, due to the large number of parameters and the even larger number of possible combinations, part variation and lack of repeatability do occur [5]. Guo et al. [6] have shown that with a constant energy input, variations to microstructure and part properties occur due to the variation in the melt pool size and geometry. Indeed, many commercial machines allow open parameter operation, whereby operators select their own process parameters. This approach gives greater control to the end user and is useful for researching new materials and structures. However, the operator is required to have a deep understanding of how parameter variation will affect the final quality of the parts being produced.

Energy density is commonly used to evaluate the effect of the process parameters on porosity and is often linked to the mechanical properties of the built parts [5, 7–10]. Energy density, E_D , is energy per unit volume applied to the powder along the intended track and is expressed as:

$$E_D = \frac{P}{HTV} \quad (1)$$

where P is laser power; H , hatch spacing; T , layer height; and V , laser scanning speed. Hatch spacing is the distance between parallel tracks. Typical units for E_D are J/mm^3 . Energy density is useful for energy comparison purposes. However, energy density does not clearly distinguish what type of defect can occur. Prashanth et al. [11] demonstrated the shortcomings of using energy density for defect predictions with an Al-Si alloy; therefore, it is not recommended to use energy density as the sole criterion for defect prediction.

Mukherjee et al. [12] refer to a lack of fusion index, referred to here as L_{F1} , and given as

$$L_{F1} = \frac{D}{T} \quad (2)$$

where D is the depth of the melt pool. The lack of fusion index needs to be greater than unity ($L_{F1} > 1$) for successful layer bonding. In this case, the melt pool created has insufficient depth to melt the powder layer and the underlying substrate. This is likely to lead to catastrophic delamination rather than singular LOF defects. Johnson et al. [13] showed a similar approach to LOF defect prediction but assumed that the ratio of depth to layer height should be greater than 1.5. But, as with ref. [12], the criterion of Johnson et al. ignores the important role of hatch spacing.

As highlighted in Eq. (2), the melt pool depth should be sufficient to melt the powder layer down to the substrate level. That being the case, LOF defects may occur when the melt pool width is insufficient compared to the hatch spacing. In this case, even though they may have

bonded sufficiently to the substrate, a lack of fusion occurs between adjacent tracks. Increasing the energy density does not guarantee a sufficiently wide melt pool, especially in cases where the hatch spacing is too large. Indeed, any increase in energy density is more likely to give greater depth rather than improved melt-pool widening. Neither L_{F1} nor E_D is sufficient in predicting LOF defects between laterally deposited tracks.

Mukherjee and DebRoy [14] have extended their non-dimensional LOF number to include a greater number of terms:

$$L_F = \frac{\rho(c_p \Delta T + L)}{\epsilon P / \pi r^2 V} F \frac{T}{D} \left(\frac{H}{W/2} \right)^2 \quad (3)$$

Here, ρ , c_p , and L represent density, specific heat and latent heat, respectively. The alloy melting range is given as ΔT . The parameters ϵ , r , and F represent the absorptivity, laser radius, and the Fourier number, respectively. W is melt pool width ($W/2$ is melt pool half-width) and D is melt pool depth. Notably, the calculation of the Fourier number requires melt pool length. Mukherjee and DebRoy developed a numerical model with heat transfer and fluid flow to estimate the width, depth, and length of the melt pool under a given set of processing conditions so that the LOF number, L_F , was calculated for selected parameters.

Following on, Mukherjee and DebRoy compared L_F to experimental results with aluminium, titanium, and stainless steel alloys. An empirical relationship has been proposed for all alloys investigated whereby the experimental void fraction, V_E , was shown to follow a linear relationship against L_F as follows:

$$V_E = 15.3L_F \quad (4)$$

A particular outcome of this analysis is that void fraction is always predicted since L_F cannot be zero.

An alternative LOF criterion, presented by Tang et al. [7], takes account of the lack of fusion between adjacent tracks and the substrate. It is given as a geometrical expression based on melt pool geometry as follows

$$\left(\frac{H}{W} \right)^2 + \left(\frac{T}{D} \right)^2 \leq 1 \quad (5)$$

where W is the melt pool width and D is the melt pool depth. Essentially, when plotted on appropriate axes, this LOF criterion follows the equation of a unit circle with the height ratio (T/D) plotted on the vertical axis and hatch ratio (H/W) plotted on the horizontal. If an operating point, whose coordinates on the graph are given as $\left(\frac{H}{W}, \frac{T}{D} \right)$, lies within the unit circle, then LOF is expected to be avoided. If the operating point lies outside the circle, then LOF is predicted.

Equation (3) is useful in its own rite, but its usefulness can be extended by linking it to process parameters such as laser power and scan speed. Gordon et al. [4] consider the depth of the melt pool to follow a Rosenthal estimation as follows

$$D = \sqrt{\frac{2P\varepsilon}{\pi e \rho c_p V (T_{melt} - T_o)}} \quad (6)$$

where ε is absorptivity; e , Euler's number; ρ , density; c_p , specific heat capacity; T_{melt} , melting temperature; and T_o , initial substrate temperature. Since the Rosenthal model is axisymmetric, the width is taken as twice the depth.

$$W=2D \quad (7)$$

Substituting for melt pool width and depth into Eq. (5) and rearranging give the following criterion for LOF prediction:

$$P \leq \frac{(H^2 + 4T^2) \pi e \rho c_p (T_{melt} - T_o)}{8\varepsilon} V \quad (8)$$

This equation gives a straight line in P – V space with its slope being representative of constant line energy (P/V). If a P – V operating point lies below the line, then LOF is predicted. Operating points should be above this prediction line under the assumption that the laser-material interaction is in conduction mode. If line energy is too high, keyhole mode may be experienced, which is not dealt with by Eq. (8). An important caveat relating to the use of Eq. (6) relates to its approximate nature and its applicability against various materials. Tang et al. [7] demonstrate that the approximation works well for maraging steel, stainless steel, and titanium alloy Ti6Al4V but does not apply to Al–Si–Mg alloys, for example.

Keyhole porosity occurs with higher line energies [15–17] [18]. The keyhole phenomenon occurs as laser radiation begins to reflect within the melt pool causing deeper voids. Keyholes are distinctive due to their large aspect ratio with $D > W$. During keyhole operation, the leading surface of the travelling melt pool becomes unstable and collapses trapping pores deep within the solidified track [19]. The prediction of keyhole porosity has been related to the solid–liquid interface's front wall angle. The destabilisation of the solid–liquid front was observed to occur at a front-wall angle of around 77° [20].

The focus of this study is on Ti6Al4V; hence, Eqs. (6–8) are assumed to be applicable. The mechanical properties of titanium alloy components depend on microstructure, porosity levels, and chemical composition [21]. Ti6Al4V is an $\alpha + \beta$ titanium alloy, and due to the rapid cooling rate during the L-PBF process, the as-built components typically exhibit an acicular $\alpha + \beta$ microstructure in a basket-weave formation.

Oftentimes, the microstructure will contain metastable α' acicular martensitic due to the high cooling rates [22][22]. The form of the microstructure influences strength and ductility [24][24]. The presence of LOF porosity has a significant impact on the mechanical performance, particularly upon the fracture and fatigue performance [26]. Khorasani et al. [27] report that for Ti6Al4V components manufactured via the L-PBF process, reductions in hardness of 100 HB and density of 5% occurred due to LOF defects. Hence, it is expected that LOF defects will impact upon other mechanical properties such as tensile strength and elongation.

In summary, various defects can occur in additive manufacturing due to the selection of process parameters and the scanning strategy employed. When line energy is too low, the most likely defects are LOF defects. LOF defects lower the mechanical properties, such as hardness, and are therefore seen as deleterious for structural applications where mechanical properties need to be maximised. Various approaches have been taken to predict LOF defects, namely energy density, the LOF indices (L_{F1} and L_F), and the Tang et al. relationship. The application of energy density for LOF prediction has been shown to be problematic (Prashanth et al. [11]). The first LOF index (L_{F1}) is, in a practical sense, related to delamination of layers rather than discrete LOF defects. Due to this limitation, Mukherjee and DebRoy developed a second, more detailed, and dimensionless number, L_F , but the application of this approach requires a sophisticated numerical model to estimate melt pool width, depth, and length. This adds considerably to the computational effort required to apply this approach. Melt pool width and depth can be measured, ex situ, on prepared metallurgical cross sections of deposited tracks. However, measurement of melt pool length is more difficult and would probably require some form of inline or in situ monitoring of the melt pool. Hence, a practical approach for validating the LOF index, L_F , is challenging and probably beyond the scope of many small-to-medium additive manufacturing production and prototyping facilities. Tang's relationship, Eq. (5), has been combined with Rosenthal predictions for melt pool geometry to give Eq. (8); however, Eq. (8) needs to be confirmed and validated against experimentally measured melt pool geometry. The measured melt pool geometry should be compared with Rosenthal predictions, and hence, the suitability of the LOF criterion given in Eq. (8) needs to be evaluated empirically. Even though there are well-known shortcomings in terms of accuracy, a particular advantage of the Rosenthal equation is its simplicity.

1.1 Aims and objectives

The aim of this study is to investigate porosity in test parts made from Ti6Al4V via the L-PBF process. The impact of hatch-spacing variation on the porosity and mechanical

properties will be established. Specifically, hardness and tensile properties will be presented for components made with different hatch spacing for which the porosity levels can be measured.

A specific objective is to adjust the hatch spacing so that the LOF prediction criteria (Eqs. (5) and (8)) can be assessed for multi-layer fabrication. Prior to multi-layer fabrication, melt pool geometry will be obtained experimentally by using single-layer depositions. These single-layer deposits shall be made using similar parameters to the multi-layer cases but will have wider hatch spacing so as to avoid track overlap. Hence, these single-layer depositions will give distinct deposition tracks whose geometry can be measured experimentally. The Rosenthal predictions of melt pool geometry will be compared against single-layer experimental values so that the LOF criterion of Eq. (8) can be evaluated directly.

The impact of any deviation between experimental data and Rosenthal predictions on the LOF criterion of Tang et al. will be assessed and recommendations for future use will be made.

2 Materials and methods

The proposed changes to the prediction criteria are outlined first, followed by the experimental fabrication and characterisation methods. All fabrication was performed using an MLab Cusing R L-PBF machine.

2.1 Modified prediction criteria

In order to generalise the relationship of Tang et al. (Eq. (5)), the following change is proposed where

$$\left(\frac{H}{W}\right)^2 + \left(\frac{T}{D}\right)^2 = R_c^2 \quad (9)$$

The terms of the equation are the same as used in Eq. (5) but with the result being equated to the squares of the radius ratio, R_c . The calculated value for R_c is a fraction of the unit radius inequality originally proposed by Tang et al.

The inputs to Eq. (9) can be derived in two ways (each with their own merits): (1) experimentally and (2) analytically.

Experimentally, by obtaining the melt pool width and depth from single-track data, we can calculate an empirically informed value for R_c (subject to change by using different hatch spacings and layer heights). After interrogation of built samples for LOF defects, we can establish an experimentally informed upper limit for R_c that need not be equal to unity ($R_c < 1$). This change to initially generalise the relationship by Tang et al. will allow for specific calibration as the next step.

Analytically, the melt pool width and depth can also be calculated by the application of the Rosenthal equation and substitution into Eq. (9) would give the generalised result for Eq. (8) as follows:

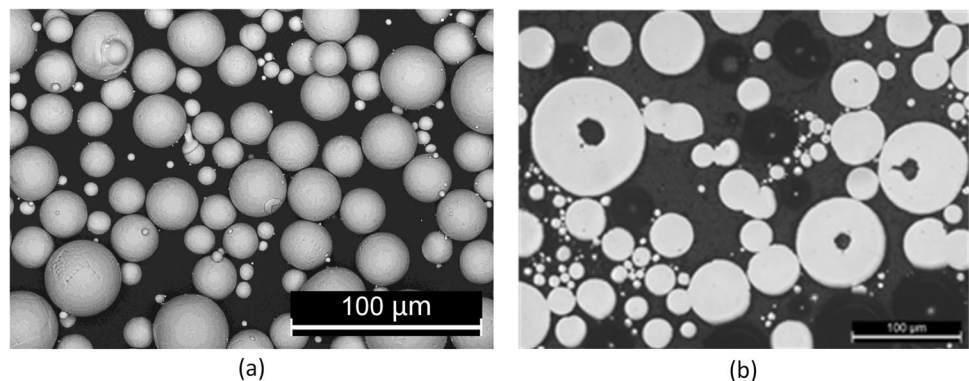
$$P < \frac{(H^2 + 4T^2)\pi e \rho c_p (T_{melt} - T_o)}{8R_c^2 \epsilon} V \quad (10)$$

In this case, the value for R_c is analytically predicted using the simplified Rosenthal equations, and differences should be expected from the empirically informed value of R_c . Nevertheless, the built samples can be interrogated for LOF defects, and the most suitable value for R_c can be established as will follow in the methodology proposed in this manuscript.

2.2 Feedstock material

Plasma-atomised Ti6Al4V powder was used throughout. Figure 1a shows a scanning electron microscope image of loose powder. There is evidence of satellite formations on some powder particles, but generally, the powder shape is spherical and deemed to be of good quality. Figure 1b shows powder that was mounted in Bakelite compound, ground, and polished with a final stage of 0.06 μm colloidal silica. Again, the circularity of the powder is good, but there is evidence of porosity within larger particles. An in-depth characterisation of the powder batch is provided elsewhere

Fig. 1 Powder images: **a** back-scattered electron microscopy image of loose powder and **b** optical image of mounted, ground, and polished powder. Spherical powder with evidence of satellites in **a** and gas porosity is evident in **b**



by Harkin et al. [28] (as the powder used here came from the same initial stock that was used in this prior work). Laser size diffraction showed that the particle size ranged from 14.5 to 76 μm with 85% of the powder between 25 and 50 μm . Hausner’s ratio and Carr’s index indicated good flowability. Elemental compositions were confirmed to be within specification for grade 23 (extra low interstitial) titanium alloy.

2.3 Single-layer depositions

In order to empirically assess the melt pool geometry, individual tracks were deposited onto the build plate made from a forged and annealed Ti6Al4V. Optical emission spectroscopy confirmed that the build plate was within specification for grade 5 titanium alloy. Tracks of length 5 mm were deposited side-by-side using a bi-directional or zigzag [29] scanning pattern over one layer only. Table 1 shows the process parameters used in the single-layer deposition and subsequently used throughout the entire study. During all fabrication, the chamber was continuously purged with argon to maintain oxygen levels below 0.1 wt.%. On the single-layer depositions, hatch spacing was maintained at 100 μm so that individual or non-overlapping tracks could be identified. A total of 49 tracks were deposited on the single-layer structure. The processed build plate was cross-sectioned perpendicular to the tracks. The cut surface was ground and polished in stages towards a 0.06 μm colloidal silica final step before etching with Kroll’s reagent to reveal

the melt pool structure (macroetching). The geometry was measured using calibrated optical microscopy.

2.4 Multilayer L-PBF sample fabrication

A 45° cross-hatching scanning strategy was selected for the multi-layer builds. Figure 2a shows the layout of the sample parts on the build plate (of size 91 × 91 mm). The samples included a variety of characterisation components numbered with respect to their position on the plate. The Recoater blade and gas flow direction are as shown in Fig. 2a. The cylindrical parts numbered 1 to 4 (10 mm in diameter and 70 mm tall (as shown in Fig. 2b) were subsequently machined and used for tensile testing. The central cylindrical part, number 5 in Fig. 2a, was used for hardness measurements. The four 8-mm cubic samples (with detail shown in Fig. 2c) were used for porosity analysis. Four builds with the same geometry, labelled as builds #1 to #4, were fabricated using the process parameters from Table 1 but combined with different levels of hatch spacing. Table 2 shows the hatch spacing variation against each build number. Build#1 had the largest hatch spacing at 100 μm , and build #4 had the smallest hatch spacing at 60 μm .

After fabrication, the as-built components on the build platform were subjected to a stress-relieving heat treatment (soaked at approximately 694 °C for 2 h followed by furnace

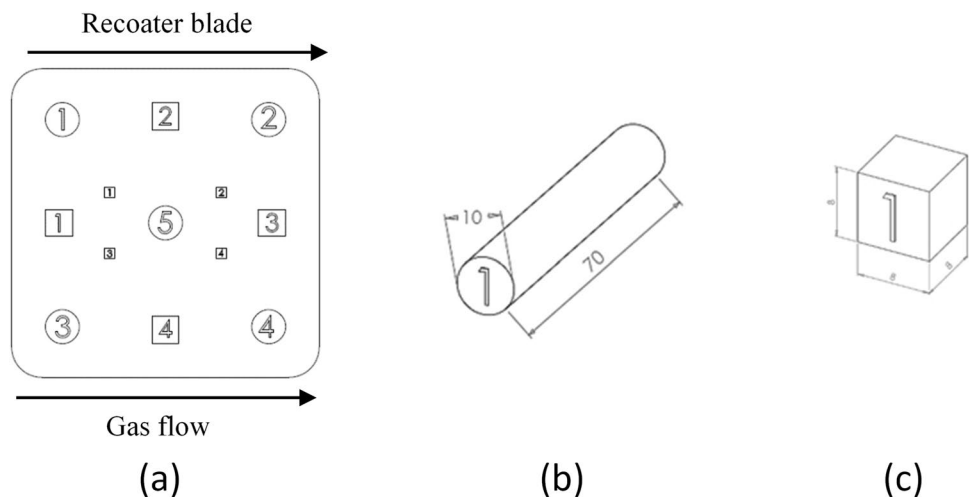
Table 1 Constant processing parameters

Laser power (W)	Spot size (μm)	Scan speed (mm/s)	Layer height (μm)
95	50	900	25

Table 2 Hatch spacing used on each build

Build no	Hatch spacing (μm)
#1	100
#2	80
#3	70
#4	60

Fig. 2 The build layout details: **a** plan view of the part layouts with Recoater blade and gas flow directions shown, **b** geometry of a cylinder sample (5 off), and **c** a typical cubic sample. four larger cubes with 8 mm sides and four smaller with 4 mm sides shown in **a**



cooling to room temperature). The samples were removed from the build plate by electric discharge machining.

2.5 Porosity analysis and mechanical testing details

Cubic components were sectioned along their mid-plane, parallel to the build plate surface (i.e. their XY plane) and prepared for porosity analysis via optical microscopy. The samples were mounted in Bakelite and ground using graduated levels of silicon carbide papers, polished using 3 μm diamond suspension, and finished with 0.06 μm colloidal silica suspension. Optical micrographs of the cross sections were acquired using bright-field optical microscopy at various magnification levels. Image processing was applied to obtain the area fraction at the macroscale of the part on the XY planes. For close-up views of the pores, scanning electron microscopy using secondary electrons (SEM-SE) was used. CT scanning was used on one sample built at 100 μm (build #1). This gave a 3D representation of the structure of the porosity.

Micro Vickers hardness testing was performed using a load of 1000 gf and a dwell time of 10 s. In preparation for hardness testing, polishing was performed using the steps as described previously. Hardness measurements were taken on the central cylinder (cylinder 5 in Fig. 2a) along its centre line and in the XZ plane. The distances between each indent were kept to 1 mm with 65 indents typical per sample.

The four cylindrical samples for tensile testing were machined to produce test bars in accordance with the ASTM E8/M. The tensile tests were undertaken with a strain rate of 1 mm/min.

2.6 Microstructure characterisation

All builds were analysed for microstructure using scanning electron microscopy–backscattered electron (SEM-BSE) imaging on parts that were cross-sectioned and polished on their XY plane to get representative microstructures.

3 Results

3.1 Single-layer results

Figure 3 shows an example of the macroetching of the single-layer track depositions. The as-deposited melt pools are bright and distinct from the wrought Ti64 substrate. The melt pools show typical microstructure for additively manufactured titanium alloy, namely acicular $\alpha + \beta$ (known as basket weave). The build plate is an equiaxed α structure with intergranular β typical of wrought titanium alloy (solution treated and overaged) [30]. Melt pool widths and depths were measured over 39 tracks, which gave the statistical data

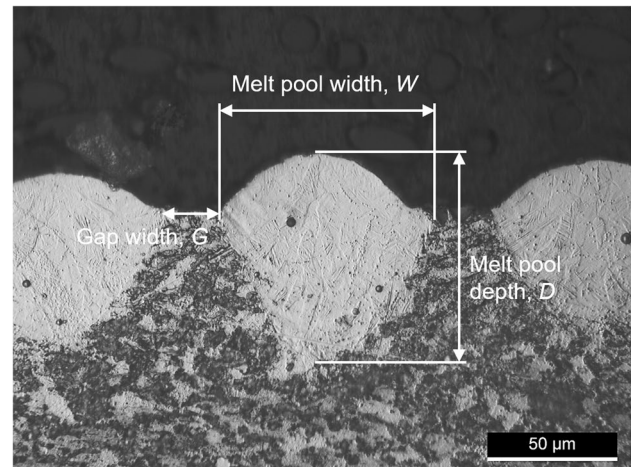


Fig. 3 Typical melt pool created from the single-layer build. Baseline process parameters were used (ref. Table 1.) with a hatch spacing of 100 μm . Major dimension annotated: melt pool width, W , depth, D and gap between tracks, G

Table 3 Melt pool measurements from single-layer build (statistics calculated over a sample size of $n=39$)

Measurements	Values (mean \pm SD)
Melt pool width, W (μm)	81 ± 4
Melt pool depth, D (μm)	71 ± 7
Gap width, G (μm)	21 ± 4

(mean values and variance) provided in Table 3. In addition, the gap widths or smallest distances between neighbouring melt pools were measured and are also summarised as the measured parameter G .

Figure 4 shows the graphical representation of the melt pool ratios in the context of the LOF criterion (Eq. 9) using experimentally obtained melt pool widths. Hatch spacing is the parameter variation. Build #1 exceeds the LOF criterion of Tang et al. (i.e. exceeds unity) by a margin of 0.65. Build #2 exceeds the criterion by a smaller margin of 0.1. Builds #3 and #4 are comfortably within the criterion (i.e. less than unity) and are therefore predicted to be free of LOF defects.

3.2 Quantitative porosity analysis

Figure 5 shows the results from porosity measurements (percentage area fractions) versus hatch spacing. The mean porosity fraction (approx. 4%) with a hatch spacing of 100 μm (i.e. build #1) is significantly higher than those obtained for 80, 70, and 60 μm (builds #2, #3, and #4). Mean porosity at a hatch spacing of 80 μm was approximately 0.05%. The mean porosity for hatch spacings at 70 and 60 μm was less than 0.01%.

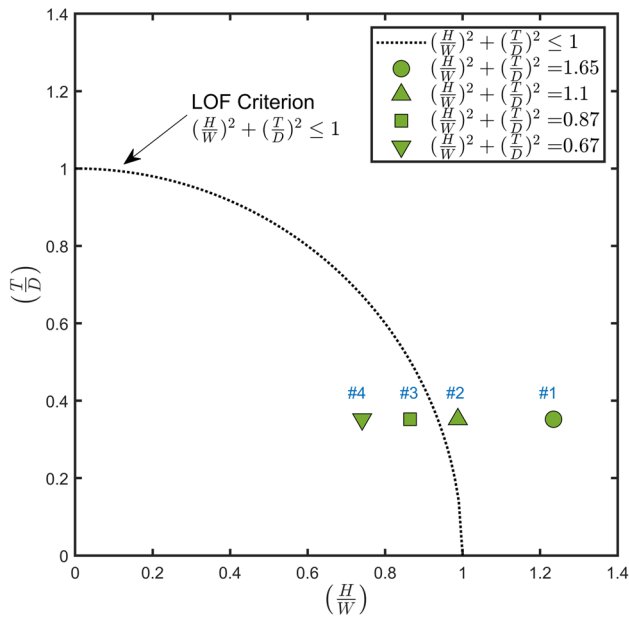


Fig. 4 Lack of fusion criterion plot with the values of R_c^2 being provided in the legend

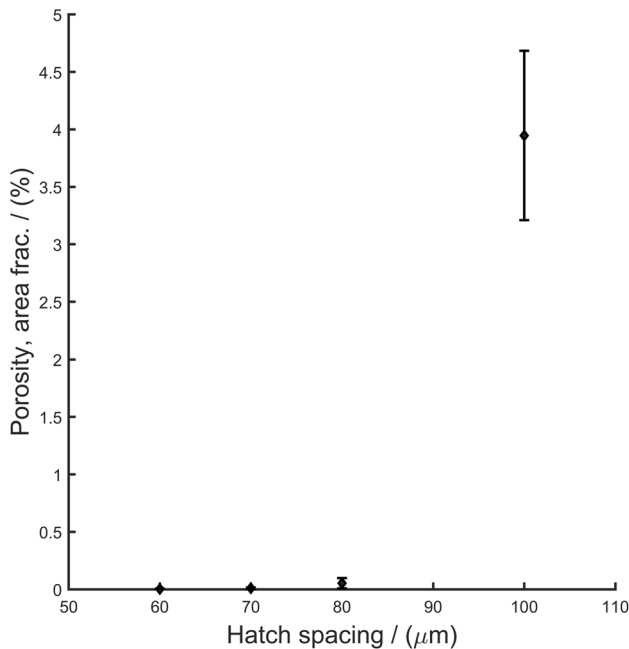


Fig. 5 Mean porosity versus hatch spacing with Standard error. Porosity was measured as area fraction (%) on the horizontal XY plane

3.3 Qualitative porosity analysis

Figure 6 shows the nature and the distribution of the porosity from build #1. Specifically, Fig. 6a shows the results of

the CT scan, and the 3D nature of the porosity is shown to be a set of vertically aligned defects. Figure 6b shows a cross section in the XY plane where the pores are regularly spaced at the intersections of the 45° cross-hatched, laser scanning directions. Figure 6c shows a cross section in the XZ direction where the vertically aligned nature of the defects is shown clearly. The defects are typically $24 \pm 3 \mu\text{m}$ in length when viewed on the XY plane and are regularly spaced at a distance of $144 \pm 5 \mu\text{m}$ measured in horizontal and vertical directions. These defects are systematic and linked to the scan strategy.

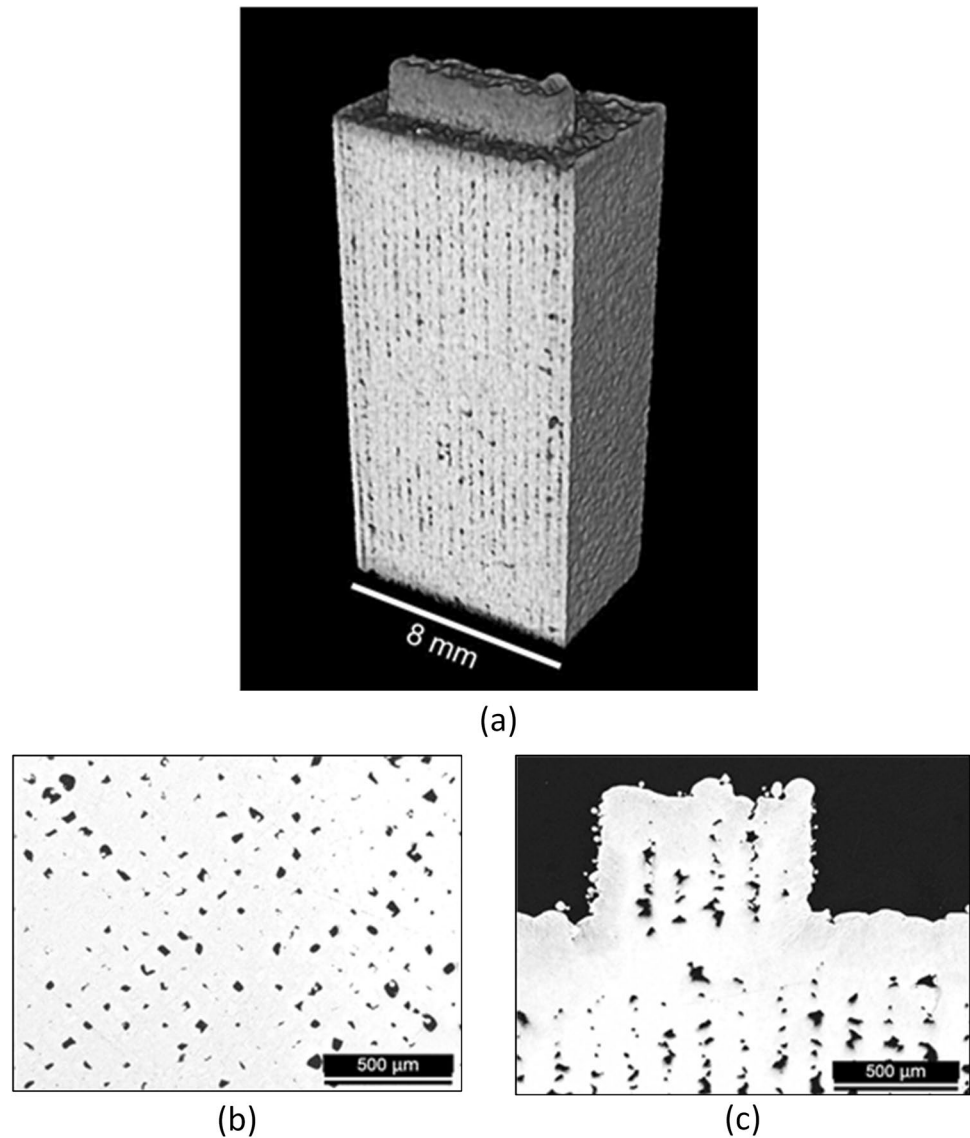
Figure 7 shows the representative polished cross section from builds #2, #3, and #4. The top row ((a) to (c)) shows the horizontal cross sections in the XY plane. The bottom row ((d) to (f)) shows the vertical cross sections in the XZ plane. The porosity in Fig. 7 is clearly much lower than that shown in build #1 (Fig. 6). In the horizontal XY planes, all pores appear to be randomly distributed. In other words, it is difficult to establish if defects are systematically linked to the scanning strategy as is expected in cases of LOF defect. However, the vertical XZ cross section of build #2, Fig. 7 (d), shows a string of vertically aligned pores which is representative of the systematic presentation of LOF defects under a cross-hatch scanning strategy. Otherwise, pores for builds #3 and #4 are so few in number that they appear to be randomly positioned.

Figure 8 shows the morphology of selected pores in builds #1 and #2. Unmelted powder particles can be seen in Fig. 8a which is from build #1. The unmelted powder particles are clear evidence of partial melting of the feedstock and therefore representative of a lack of complete fusion of the powder. Figure 8 b and c show another type of pore that was found occasionally in the analysis, a tunnel defect. The tunnel defects show no powder particle within (as they may have been removed during polishing), but it has a roughly diamond or lozenge shape that is aligned with the 45° alternating scanning strategy. Both types of pore were found throughout builds #1 and #2, which would suggest that both pore types are typical of LOF defects. The main difference between tunnel defects seen in builds #1 and #2 was their size. Pores in build #1 are routinely larger than those found in build #2. The change in size is due to the change in hatch spacing value from 100 μm in build #1 to 80 μm in build #2. Reducing the hatch spacing significantly reduces the gap width, G in Fig. 3, which decreases the size of the defect as clearly shown in Fig. 8

Pores in builds #3 and #4 were very few in number but of those analysed, very few shared the characteristics shown in Fig. 8.

It can be concluded that builds #1 and #2 showed clear evidence of systematic LOF defects through association linking size, shape, and distribution with the 45° alternating scanning strategy geometry. Builds #3 and #4 showed fewer,

Fig. 6 Systematic lack of fusion porosity for build #1, **a** CT scan, **b** optical image on the horizontal (XY) plane, and **c** optical image on the vertical plane (XZ)



random defects that could not be clearly associated with the scanning strategy geometry but that may be associated with initial porosity in the powder (among other sources). It is worth noting that very small random spherical pores were observed in the single-layer, solidified deposits of Fig. 3. Hence, it is recommended that the methods used here, namely CT scanning, optical microscopy on different cross sections, and SEM-SE microscopy, be used in combination to identify LOF defects, especially when the porosity level is less than 1% (as was the case for build #2).

3.4 Microstructure analysis

Figure 9 shows the microstructures observed in the XY planes of each build; the dark areas are the lamellar α

phase whereas the white areas represent the β phase. The samples were subject to post-build stress-relieving heat treatment below the β transus temperature. By comparing the microstructures of all builds, it is not possible to identify any significant difference in the morphology of the microstructures. This indicates that under fixed laser power and scanning speed, the microstructure was not altered by hatch spacing.

3.5 Mechanical properties

Figure 10 presents the Vickers hardness data for each build. The average hardness values for builds #2, #3, and #4 were found to be similar at around 385 to 395 HV, whereas the mean hardness of build #1 was significantly lower at 360

Fig. 7 Porosity from builds #2, #3, and #4. The top row (a, b, and c) shows horizontal planes, and the bottom row (d, e, and f) shows vertical. A string of vertically aligned pores can be seen in d

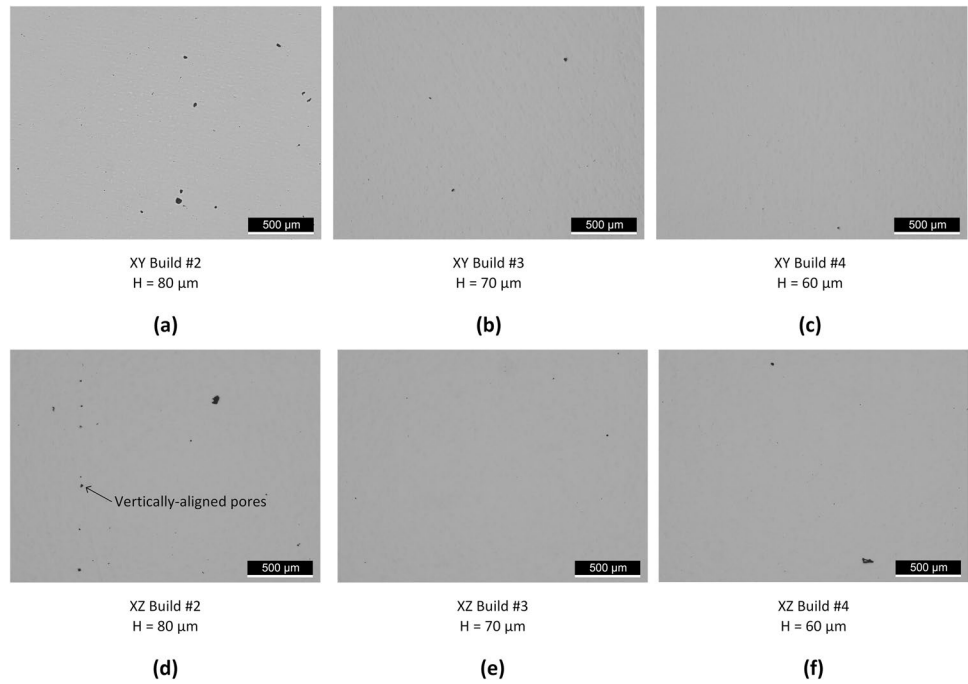


Fig. 8 Representative LOF pore morphologies in build #1 (a) and (b) and build #2 (c) captured in the XY plane by SEM-SE

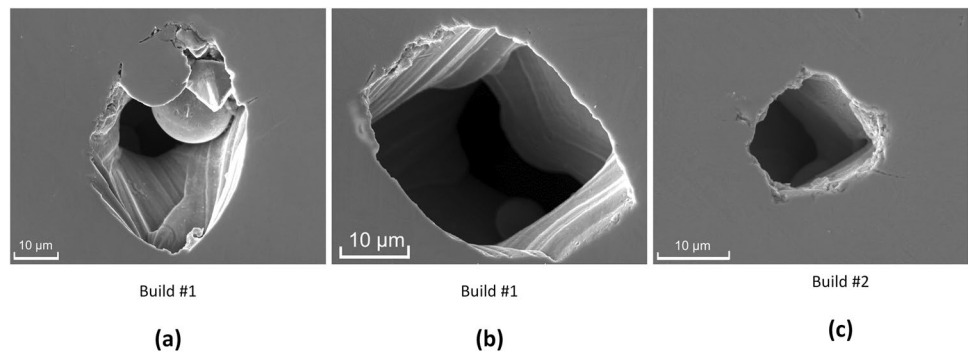
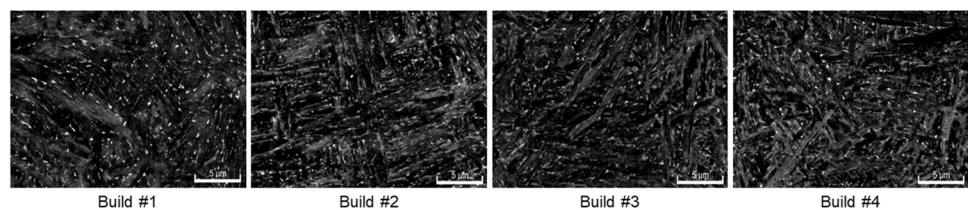


Fig. 9 SEM-BSE (under the same magnification of 10 kx) showing the microstructure of builds #1, #2, #3, and #4 observed in the X–Y plane



HV. Additionally, a higher standard deviation is shown for the data from build #1, which is relatable to the larger variances observed in the porosity data for this build number.

Figure 11 shows the tensile strength data from each multi-layer build. Similar to the trends witnessed for average hardness, there is a significant reduction in the average tensile strength for build #1 compared to others. Ductility is presented as percentage elongation in Fig. 12. The average elongation for build #1 was the lowest of all cases at around 6%.

Table 4 summarises the mechanical properties gathered with mean values and standard error of means where

applicable. In addition, the results for the LOF criteria described by Eq. (5) are provided.

4 Discussion

4.1 Single-layer results

The single-layer tracks showed good uniformity in their geometry. Since depth was consistently less than width, the melt pools are considered typical of conduction mode

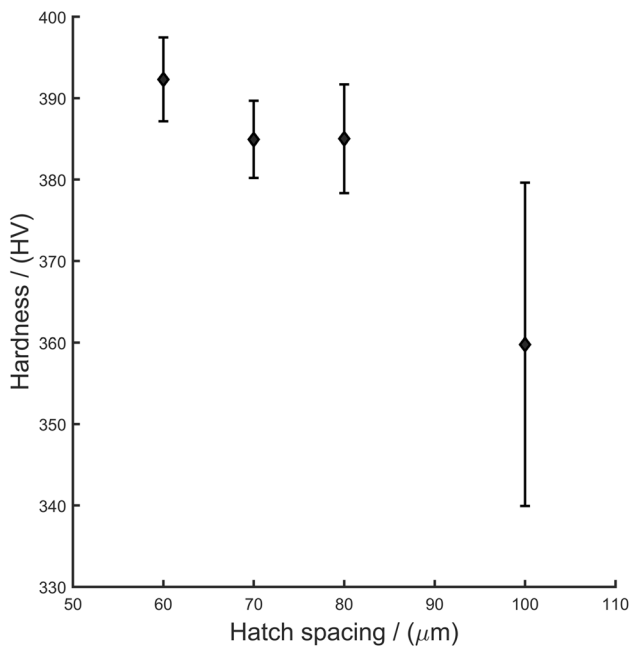


Fig. 10 Vickers hardness versus hatch spacing of the built parts measured on the XY plane. Error bars represent the standard deviation

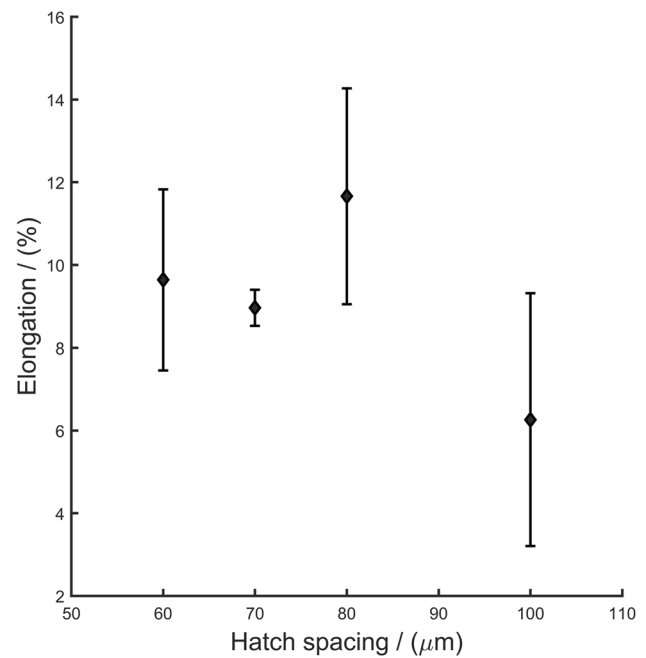


Fig. 12 Elongation versus hatch spacing for the cylindrical parts. Error bars represent the standard deviation

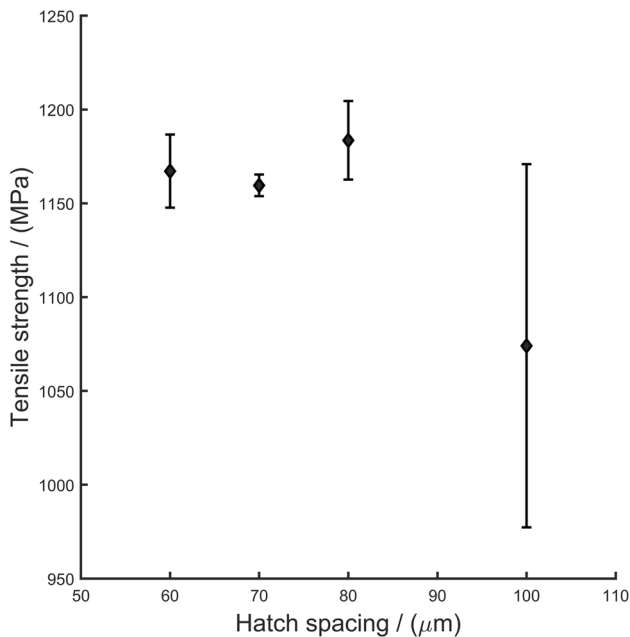


Fig. 11 Tensile strength versus hatch spacing for the cylindrical parts. Error bars represent the standard deviation

operation; that is, no keyhole formation had occurred. Clear gaps were present between all melt pools with an average gap distance of 21 μm . The sum total of the average melt pool width and average gap distance was 102 μm , which

equates sufficiently well to the hatch spacing of 100 μm (as expected). The question arises on whether the tracks were sufficiently far apart to avoid thermal interaction, in other words, did the presence of a warm prior track increase the initial temperature for its new neighbour and hence influence the melt pool geometry? Thermal modelling was performed using a bespoke heat conduction FEA model that is described elsewhere [31]. The model showed melt pool geometry stabilising over four tracks. From the model's initial track to its fourth track, the depth changed from 69.6 to a steady value of 72.8 μm . Likewise, the model's predicted melt pool width changed from 78.4 to 81.2 μm . The thermal model's temperature data showed predictions of preheating to around 377 $^{\circ}\text{C}$ for the fourth track just prior to deposition. However, as just described, the impact of this preheating on the final melt pool geometry was of the order of microns and is similar in scale to the standard deviation reported in Table 3. Therefore, the changes in the predicted melt pool geometry over the first four tracks can be assumed to have been negligible. Adjacent tracks at this oversized hatch spacing can therefore be considered to have experienced negligible thermal interaction.

Denudation of powder can influence the final deposition geometry of adjacent tracks where the first track with no denudation effect can in some cases be observed to have greater track height compared to subsequent tracks [32]. After inspection, there was no evidence of significant height change or denudation effects in our experimental case. Therefore, the melt pool

Table 4 Summary of main findings (mean with standard errors, where appropriate)

Build no	Hatch spacing (μm)	R_c^2 (Eq. (9) (-)	Porosity fraction (%)	Hardness (HV)	Tensile strength (MPa)	Elongation (%)
#1	100	1.65	3.95 ± 0.43	360 ± 2.5	1074 ± 56	6.3 ± 1.8
#2	80	1.10	0.05 ± 0.01	385 ± 0.8	1184 ± 11	11.7 ± 1.3
#3	70	0.87	0.01 ± 0.002	385 ± 0.6	1160 ± 3	9.0 ± 0.3
#4	60	0.67	0.003 ± 0.001	392 ± 0.6	1167 ± 11	9.6 ± 1.3

measurements acquired experimentally can be deemed to be representative of the melt pool geometry created under the operating conditions (laser power and scan speed) used throughout the study.

4.2 Porosity analysis and its effects on mechanical properties

There were clear differences between the porosity area fraction for build #1 and the other three cases. Build #1, with a hatch spacing of 100 μm , showed clear systematic LOF defects at a porosity fraction of around 4%. These LOF defects in build #1 were approximately 21 μm in size, which is equal to the mean gap distance, G , measured between melt pools for the single-layer depositions also at a hatch spacing of 100 μm . The nearest neighbour distances between flaws in build #1 were uniform and approximately equal to 144 μm . Considering that a 45° cross-hatching laser scanning strategy was used, the distance between track intersection points on subsequent layers was expected to be around $\sqrt{2}H$ (i.e. the diagonal of a square with sides equal to H). In the case of build #1, $\sqrt{2}H = 141 \mu\text{m}$, which is sufficiently close to 144 μm to confirm that defects are systematically associated with the hatch spacing used in the scanning strategy.

Buids #2, #3, and #4 showed similar porosity percentages to each other, that is, stochastic porosity with area fractions less than 0.1%. However, on deeper analysis using cross sectioning with optical microscopy and SEM-SE imaging, build #2 was confirmed with evidence of systematic LOF defects, namely alignment of pores in the vertical direction and having the morphologies associated with Fig. 8 (both types of pore).

Buids #3 and #4 showed less defects that were confirmed as being representative of neither LOF nor keyhole porosity. They shared more characteristic resemblances with gas porosity. Gas porosity was observed within the original powder feedstock (see Fig. 1b). According to Gordon et al. [4], approximately 90% of the initial gas porosity in powder can be eliminated through the L-PBF process, which infers a 10% survival rate for powder gas porosity in the final part. Sinclair et al. [19] discuss other sources of gas within the L-PBF process. Hydrogen, which is twice as

soluble in liquid as in solid, can be rejected from solid into the melt as the solidification front advances. Hydrogen, it is suggested [33], comes from the decomposition of physisorbed water molecules or chemisorbed hydroxides in the powder or from the decomposition of water vapour in the build chamber. Harkin et al. [34] have reported elsewhere on the analysis of sieved powder from an instance of build #1. They showed evidence of hydrogen in sieve-captured powder. Even though the sieving and blending processes significantly reduced the interstitial elements, given the evidence that hydrogen was found in the discarded powder, it is likely that small amounts of soluble hydrogen found their way into parts and contributed to the random porosity.

The mechanical properties of build #1 were clearly adversely affected by the presence of LOF defects compared to the other build cases. Build #2, which showed clear evidence of LOF defects, was shown to have performed comparably well in its mechanical properties to builds #3 and #4. Hence, build #2 gives a threshold level where LOF defects begin to appear but, due to the low occurrence and their small size, do not adversely affect the mechanical properties. Hardness, tensile strength, and elongation were all significantly reduced and had significantly higher variances when LOF defects were present at the level found in build #1.

It has been shown elsewhere [35] that the level of interstitial oxygen has an effect on the mechanical performance of parts made with reused powder in a top-up regime. In that previous study, the effect of elevated interstitial oxygen increased the hardness and the tensile strength but reduced the elongation considerably. The results shown here demonstrate that the reduction in porosity improved hardness, tensile strength, and elongation. The oxygen levels were tested across all samples with low variation in results and all within the grade 23 composition requirement. Hence, the change in the mechanical properties in this instance could not be attributed to oxygen pick up nor due to microstructural differences, but could only be attributed to changes in the porosity level as a function of hatch spacing. Needless to say, if oxygen levels were increased significantly, then this would alter further the mechanical properties, but high oxygen content was confirmed not to be the case in the current study.

Table 5 Rosenthal predictions versus measured melt pool

Features	Rosenthal prediction	Measured	Difference (%)
Melt pool width, W (μm)	113	81	+ 32 (40%)
Melt pool depth, D (μm)	56	71	– 15 (21%)

Table 6 Comparison of LOF criteria, Eq. (3) based experimentally measured melt pool geometry and predicted geometry through the Rosenthal-based approximation

Build no	LOF criterion, R_c^2 (experimental)	R_c (experimental)	LOF criterion, R_c^2 (analytical)	R_c (analytical)
#1	1.65	1.28	0.99	0.99
#2	1.10	1.05	0.70	0.83
#3	0.87	0.93	0.58	0.76
#4	0.67	0.82	0.48	0.69

4.3 Rosenthal melt pool geometry prediction

Results from Rosenthal estimates of melt pool depth and width (Eqs. (6) and (7)) are summarised in Table 5 along with the observed differences when compared to measured values. The melt pool width is overestimated by 40% or 32 μm , whereas the depth is underestimated by 21% or 15 μm . This overestimate in width is consistent with the findings of Promopattum et al. [36], who compared Rosenthal to numerical and experimental data and showed that the analytical Rosenthal equation overestimates width over a range of high energy densities. The depth prediction from Rosenthal's equation is an underestimate by 21%. This underestimate in height is simply explained by the fact that Rosenthal's equation ignores added material, i.e. the melt pool is assumed to be collinear with the substrate surface (similar to welding without a filler material). The remelted depth measured from the build plate's top surface is 52 μm , and this is sufficiently close to Rosenthal's prediction of depth at 56 μm .

The errors in the Rosenthal predictions lead to an adverse effect on the LOF prediction criteria and the P – V prediction Eq. (8). These effects are discussed in the proceeding section.

4.4 Lack of fusion prediction criteria

The results from the second LOF criterion, Eq. (9), are shown graphically in Fig. 4 and are listed in Table 6 for convenience. Using the experimentally measured melt pool geometry, LOF defects are successfully predicted using the original relationship of Tang et al. (Eq. 5) in build #1 since the criterion is 1.65 and is greater than unity. The level of defects in build #1 significantly affected the mechanical properties in a negative way. Tang's original criterion predicted LOF defects in build #2 with

a criterion value of 1.1 or an $R_c = 1.05$. LOF defects were observed in build #2 but, as discussed previously, due to their low size and distribution level, their impact on the mechanical properties appeared to be marginal. The LOF criterion values for builds #3 and #4 are well within Tang's original criterion of the unit, and this is shown in the final results as LOF defects appeared to be absent in both of these cases.

As shown in Table 6, substitution of the predicted Rosenthal melt pool geometry values into the LOF criterion gave values below unity in all cases (albeit marginally so for build #1). Hence, LOF was not predicted in any case using Rosenthal estimates for melt pool geometry. This finding has significant implications for the applicability of Eq. (8) in its present form.

If analytical predictions are to be used (i.e. Rosenthal equations), then this analysis suggests that the LOF criterion of Eq. (9) should be adjusted with $R_c = 0.83$ or $R_c^2 = 0.7$. This criterion value is selected to be less than build #2 conditions, since build #2 was shown to have LOF defects but at the point where marginal adverse impact was observed on the mechanical properties. Hence, build #2 represents a threshold ceiling value. Calibration of the P – V prediction Eq. (10) is also necessary and is modified by substituting with $R_c^2 = 0.7$ to give:

$$P < \frac{(H^2 + 4T^2)\pi e \rho c_p (T_{melt} - T_o)}{5.6\epsilon} V \quad (11)$$

Equation (11) is applied to the current data and is presented in the P – V diagram of Fig. 13. (The relevant physical property data are taken from Gordon et al. [4].) The updated LOF criterion at each level of hatch spacing is shown along with the P – V operating point of the multilayer fabrication. Each line on the plot represents a specific line-energy value.

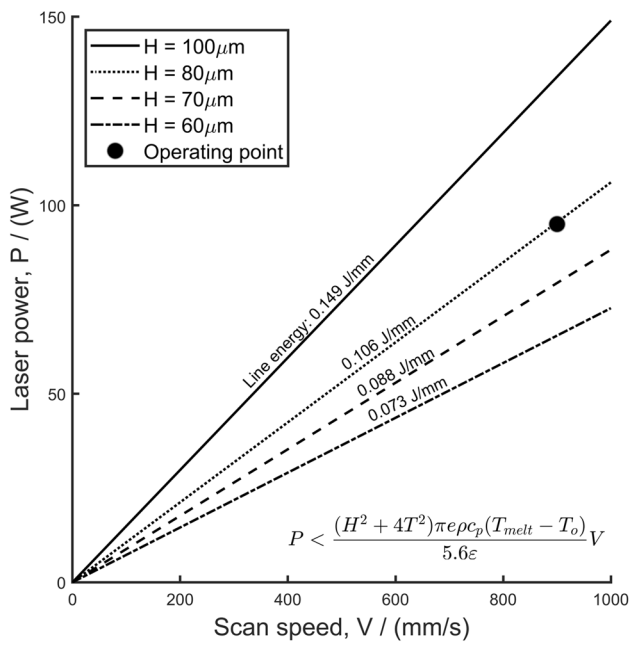


Fig. 13 The updated LOF criterion plotted on the P – V space. The plots show line energies for various hatch spacing based on the modified criterion of $R_c^2 = 0.7$

This adaptation to the P – V criterion is the simplest modification possible. If melt pool width and depth predictions can be improved by more advanced means (such as numerical modelling), then LOF prediction and avoidance will improve also. One particular phenomenon that is known to impact on melt pool geometry is called Marangoni convection. Surface tension gradients in the melt drive convection in the melt pool, which, in turn, tends to increase the melt pool width yet decrease the depth [37]. The accurate prediction of these effects will require computational fluid mechanics models coupled with solidification.

5 Conclusion

The aim of this study was to investigate porosity in multilayer test parts made from Ti6Al4V via the L-PBF process. Hatch spacing was used as the main parameter adjustment in order to evaluate LOF porosity. Four builds with the similar processing parameters but each with different levels of hatch spacing at 100, 80, 70 and 60 μm , respectively, were carried out. All components were subjected to a stress relief thermal cycle, which was conducted below the β transus temperature.

With hatch spacing set at 100 μm , LOF defects were observed at an overall porosity fraction of 3.95%. For all other cases with lower hatch spacing, the porosity fractions were much less than 1%. With LOF defects present to the level of 3.95%, the hardness dropped by 30

to 360 HV; tensile strength dropped by 110 to 1074 MPa; and elongation reduced from around 10% to an average of 6.3%. Indeed, all of the tensile test bars with LOF defects failed with little or no necking in the tensile test specimens. The LOF defects caused an increase in the variance of the mechanical properties, which will reduce the reliability of components in service.

The LOF prediction criteria of Tang et al. [7], Eq. (5), were generalised by equating to R_c^2 and evaluated using alternative melt pool geometry estimates: (1) using experimentally measured melt pool geometry from single-layer depositions and (2) using predicted melt pool geometry estimated from analytical (Rosenthal) theory. For the case with hatch spacing set at 100 μm and 80 μm , LOF defects were present as predicted by Tang’s relationship (using empirically measured melt pool width and depth). Tang’s LOF criterion successfully predicted the absence of LOF defects for cases with hatch spacing set at 70 and 60 μm . Hence, in this case, the geometry-based LOF criterion of Tang et al. when used in combination with experimentally measured melt pool geometry is deemed useful in predicting LOF defects. However, further data should be generated to confirm this case.

Gordon et al. [4] suggest that the Tang geometrical LOF criterion (Eq. (5)) can be used in combination with Rosenthal predictions of melt pool geometry (that is, melt pool width and depth). It was discovered that the Rosenthal-based approach overestimated melt pool width by 40% and underestimated the depth by 21%, which in turn, meant that the Rosenthal-informed LOF criterion failed to predict LOF defects in all cases. If a Rosenthal approach is to be used for LOF prediction, then this study suggests that the parameter of R_c^2 should be introduced (Eq. (10)) with a value of R_c^2 less than unity. This correction was applied to give an updated estimation of LOF operating parameters in P – V space. Equation (11) gives the updated LOF criterion that relates minimum laser power to scan speed for predicting LOF avoidance.

In summary, LOF defects have deleterious effects on the mechanical properties of Ti6Al4V (even after stress relief treatment) and should be avoided in structural components. The LOF prediction criterion of Tang et al. [7] used with experimentally measured melt pool geometry as inputs was found to be an adequate approach to LOF prediction and avoidance. However, the same criterion when used with analytically derived melt pool geometry was found to be problematic. An updated version of the LOF criterion with a lower inequality threshold value of $R_c = 0.83$ or $R_c^2 = 0.7$ is proposed for the case with an analytical estimation. This change to the LOF criterion is extended to give a modified P – V relationship for LOF avoidance (as shown in Eq. (11)). The proposed modification gives a simple yet very useful adaptation for Ti6Al4V alloy L-PBF components that can be verified on a case-by-case basis as required.

Author contribution All authors contributed to the study's conception and design. Material preparation, data collection, and analysis were performed by Ryan Harkin, Hao Wu, Sagar Nikam, Shuo Yin, Rocco Lupoi, and Shaun McFadden. Access and use of manufacturing equipment were provided by Patrick Walls and Wilson McKay. The first draft of the manuscript was written by Ryan Harkin, and all authors commented on previous versions of the manuscript. All authors read and approved the final manuscript.

Funding This research (authors RH, HW, SN, SMF) leading to these results received funding from INTERREGVA (Project ID: IVA5055, Project Reference Number: 047). The North West Centre for Advanced Manufacturing (NW CAM) project is supported by the European Union's INTERREG VA Programme, managed by the Special EU Programmes Body (SEUPB). The views and opinions in this document do not necessarily reflect those of the European Commission or the Special EU Programmes Body (SEUPB). Catalyst based in Northern Ireland may be contacted for further information in relation to the NW CAM project.

Availability of data and materials This manuscript has no associated data to be deposited.

Code availability Not applicable.

Declarations

Ethics approval Not applicable.

Consent to participate Not applicable.

Consent for publication Not applicable.

Competing interests Authors Ryan Harkin, Hao Wu, Sagar Nikam, Shaun McFadden, Shuo Yin, Rocco Lupoi have no competing interests to declare that are relevant to the content of this article. Authors Patrick Walls and Wilson McKay receive a salary from Laser Prototype Europe who provided access to their equipment for the purpose of this study.

Open Access This article is licensed under a Creative Commons Attribution 4.0 International License, which permits use, sharing, adaptation, distribution and reproduction in any medium or format, as long as you give appropriate credit to the original author(s) and the source, provide a link to the Creative Commons licence, and indicate if changes were made. The images or other third party material in this article are included in the article's Creative Commons licence, unless indicated otherwise in a credit line to the material. If material is not included in the article's Creative Commons licence and your intended use is not permitted by statutory regulation or exceeds the permitted use, you will need to obtain permission directly from the copyright holder. To view a copy of this licence, visit <http://creativecommons.org/licenses/by/4.0/>.

References

- Sutton AT, Kriewall CS, Leu MC et al (2020) Characterization of laser spatter and condensate generated during the selective laser melting of 304L stainless steel powder. *Addit Manuf* 31:100904. <https://doi.org/10.1016/j.addma.2019.100904>
- Thijs L, Verhaeghe F, Craeghs T et al (2010) A study of the microstructural evolution during selective laser melting of Ti–6Al–4V. *Acta Mater* 58:3303–3312. <https://doi.org/10.1016/j.actamat.2010.02.004>
- DebRoy T, Wei HL, Zuback JS et al (2018) Additive manufacturing of metallic components – process, structure and properties. *Prog Mater Sci* 92:112–224. <https://doi.org/10.1016/j.pmatsci.2017.10.001>
- Gordon JV, Narra SP, Cunningham RW et al (2020) Defect structure process maps for laser powder bed fusion additive manufacturing. *Addit Manuf* 36:101552. <https://doi.org/10.1016/j.addma.2020.101552>
- Dowling L, Kennedy J, Shaughnessy SO, Trimble D (2020) A review of critical repeatability and reproducibility issues in powder bed fusion. *Mater Des* 186:108346. <https://doi.org/10.1016/j.matdes.2019.108346>
- Guo Q, Zhao C, Qu M et al (2019) In-situ characterization and quantification of melt pool variation under constant input energy density in laser powder bed fusion additive manufacturing process. *Addit Manuf*. <https://doi.org/10.1016/j.addma.2019.04.021>
- Tang M, Pistorius PC, Beuth JL (2017) Prediction of lack-of-fusion porosity for powder bed fusion. *Addit Manuf* 14:39–48. <https://doi.org/10.1016/j.addma.2016.12.001>
- Gong H, Rafi K, Gu H et al (2014) Analysis of defect generation in Ti–6Al–4V parts made using powder bed fusion additive manufacturing processes. *Addit Manuf*. <https://doi.org/10.1016/j.addma.2014.08.002>
- Verlee B, Dormal T, Lecomte-Beckers J (2012) Density and porosity control of sintered 316L stainless steel parts produced by additive manufacturing. *Powder Metall*. <https://doi.org/10.1179/0032589912Z.00000000082>
- Kasperovich G, Haubrich J, Gussone J, Requena G (2016) Correlation between porosity and processing parameters in TiAl6V4 produced by selective laser melting. *Mater Des*. <https://doi.org/10.1016/j.matdes.2016.05.070>
- Prashanth KG, Scudino S, Maity T et al (2017) Is the energy density a reliable parameter for materials synthesis by selective laser melting? *Mater Res Lett* 5:386–390. <https://doi.org/10.1080/21663831.2017.1299808>
- Mukherjee T, Zuback JS, De A, DebRoy T (2016) Printability of alloys for additive manufacturing. *Sci Rep* 6:1–8. <https://doi.org/10.1038/srep19717>
- Johnson L, Mahmoudi M, Zhang B et al (2019) Assessing printability maps in additive manufacturing of metal alloys. *Acta Mater* 176:199–210. <https://doi.org/10.1016/j.actamat.2019.07.005>
- Mukherjee T, DebRoy T (2018) Mitigation of lack of fusion defects in powder bed fusion additive manufacturing. *J Manuf Process* 36:442–449. <https://doi.org/10.1016/j.jmapro.2018.10.028>
- Yang J, Han J, Yu H et al (2016) Role of molten pool mode on formability, microstructure and mechanical properties of selective laser melted Ti–6Al–4V alloy. *Mater Des* 110:558–570. <https://doi.org/10.1016/j.matdes.2016.08.036>
- Soylemez E (2020) High deposition rate approach of selective laser melting through defocused single bead experiments and thermal finite element analysis for Ti–6Al–4V. *Addit Manuf* 31:100984. <https://doi.org/10.1016/j.addma.2019.100984>
- Dilip JJS, Zhang S, Teng C et al (2017) Influence of processing parameters on the evolution of melt pool, porosity, and microstructures in Ti–6Al–4V alloy parts fabricated by selective laser melting. *Prog Addit Manuf* 2:157–167. <https://doi.org/10.1007/s40964-017-0030-2>
- Martin AA, Calta NP, Khairallah SA et al (2019) Dynamics of pore formation during laser powder bed fusion additive manufacturing. *Nat Commun*. <https://doi.org/10.1038/s41467-019-10009-2>
- Sinclair L, Leung CLA, Marussi S et al (2020) In situ radiographic and ex situ tomographic analysis of pore interactions during multilayer builds in laser powder bed fusion. *Addit Manuf* 36:101512. <https://doi.org/10.1016/j.addma.2020.101512>
- Cunningham RW, Zhao C, Parab ND et al (2019) Keyhole threshold and morphology in laser melting revealed by ultrahigh-speed x-ray imaging. *Science* (80-) 363:849–852. <https://doi.org/10.1126/science.aav4687>

21. Liu S, Shin YC (2019) Additive manufacturing of Ti6Al4V alloy: a review. *Mater Des*. <https://doi.org/10.1016/j.matdes.2018.107552>
22. Fousová M, Vojtěch D, Kubásek J et al (2017) Promising characteristics of gradient porosity Ti-6Al-4V alloy prepared by SLM process. *J Mech Behav Biomed Mater*. <https://doi.org/10.1016/j.jmbbm.2017.01.043>
23. Tao P, Li H, xue, Huang B ying, et al (2018) Tensile behavior of Ti-6Al-4V alloy fabricated by selective laser melting: effects of microstructures and as-built surface quality. *China Foundry*. <https://doi.org/10.1007/s41230-018-8064-8>
24. Xu W, Brandt M, Sun S et al (2015) Additive manufacturing of strong and ductile Ti-6Al-4V by selective laser melting via in situ martensite decomposition. *Acta Mater*. <https://doi.org/10.1016/j.actamat.2014.11.028>
25. Zhang X-Y, Fang G, Leeftang S et al (2018) Effect of subtransus heat treatment on the microstructure and mechanical properties of additively manufactured Ti-6Al-4V alloy. *J Alloys Compd* 735:1562–1575. <https://doi.org/10.1016/j.jallcom.2017.11.263>
26. Tammis-Williams S, Withers PJ, Todd I, Prangnell PB (2017) The influence of porosity on fatigue crack initiation in additively manufactured titanium components. *Sci Rep*. <https://doi.org/10.1038/s41598-017-06504-5>
27. Khorasani AM, Gibson I, Awan US, Ghaderi A (2019) The effect of SLM process parameters on density, hardness, tensile strength and surface quality of Ti-6Al-4V. *Addit Manuf*. <https://doi.org/10.1016/j.addma.2018.09.002>
28. Harkin R, Wu H, Nikam S et al (2020) Reuse of grade 23 ti6al4v powder during the laser-based powder bed fusion process. *Metals (Basel)* 10:1–14. <https://doi.org/10.3390/met10121700>
29. Jia H, Sun H, Wang H et al (2021) Scanning strategy in selective laser melting (SLM): a review. *Int J Adv Manuf Technol* 113:2413–2435. <https://doi.org/10.1007/s00170-021-06810-3>
30. Shunmugavel M, Polishetty A, Littlefair G (2015) Microstructure and mechanical properties of wrought and additive manufactured Ti-6Al-4V cylindrical bars. *Procedia Technol* 20:231–236. <https://doi.org/10.1016/j.protcy.2015.07.037>
31. Nikam SH, Wu H, Harkin R et al (2021) On the application of directional correction factors for a computationally efficient thermal model of laser-based powder bed fusion processes. submitted
32. Yadroitsev I, Bertrand P, Antonenkova G et al (2013) Use of track/layer morphology to develop functional parts by selective laser melting. *J Laser Appl* 25:052003. <https://doi.org/10.2351/1.4811838>
33. Anderson IE, White EMH, Dehoff R (2018) Feedstock powder processing research needs for additive manufacturing development. *Curr Opin Solid State Mater Sci* 22:8–15. <https://doi.org/10.1016/j.cossms.2018.01.002>
34. Harkin R, Wu H, Nikam S et al (2021) Analysis of spatter removal by sieving during a powder-bed fusion manufacturing campaign in grade 23 titanium alloy. *Metals (Basel)* 11:1–13. <https://doi.org/10.3390/met11030399>
35. Harkin R, Wu H, Nikam S et al (2022) Powder reuse in laser-based powder bed fusion of Ti6Al4V—changes in mechanical properties during a powder top-up regime. *Materials (Basel)* 15:2238. <https://doi.org/10.3390/ma15062238>
36. Promopattam P, Yao SC, Pistorius PC, Rollett AD (2017) A comprehensive comparison of the analytical and numerical prediction of the thermal history and solidification microstructure of Inconel 718 products made by laser powder-bed fusion. *Engineering* 3:685–694. <https://doi.org/10.1016/j.eng.2017.05.023>
37. Nikam SHSH, Quinn J, McFadden S (2021) A simplified thermal approximation method to include the effects of Marangoni convection in the melt pools of processes that involve moving point heat sources. *Numer Heat Transf Part A Appl* 79:537–552. <https://doi.org/10.1080/10407782.2021.1872257>

Publisher's Note Springer Nature remains neutral with regard to jurisdictional claims in published maps and institutional affiliations.